**Key Points:**

- Post-sunset enhancement in plasma density over the equatorial ionization anomaly (EIA) crest region are found during December solstice and Equinox in high solar epoch
- Pre-reversal enhancement of the zonal electric field over the dip equator causes this enhancement in about 1.7 h
- Plasma transport from 5° to 10° magnetic latitude to the EIA crest region leads to shorter response time

**Correspondence to:**

A. Kumar,
ankitprl2017@gmail.com

# Evidence for the Significant Differences in Response Times of Equatorial Ionization Anomaly Crest Corresponding to Plasma Fountains During Daytime and Post-Sunset Hours

A. Kumar[1,2] , D. Chakrabarty[1] , K. Pandey[1,3] , B. G. Fejer[4] , S. Sunda[5] , G. K. Seemala[6] , S. Sripathi[6] , and A. K. Yadav[1]

[1]Physical Research Laboratory, Ahmedabad, India, [2]Indian Institute of Technology, Gandhinagar, India, [3]Now at ISAS, Department of Physics and Engineering Physics, University of Saskatchewan, Saskatoon, Saskatchewan, Canada, [4]Utah State University, Logan, UT, USA, [5]Airport Authority of India, Ahmedabad, India, [6]Indian Institute of Geomagnetism, Navi Mumbai, India

**Abstract** Based on 10 years' (2010–2019) of vertical total electron content (VTEC) data from Ahmedabad (23.0°N, 72.6°E, dip angle 35.2°) and campaign based OI 630.0 nm airglow intensity measurements from Mt. Abu (24.6°N, 72.7°E, dip angle 38.0°), it is shown that plasma density over the equatorial ionization anomaly (EIA) crest region increases in varying degrees during post-sunset hours (2000–2100 LT) in magnetically quiet periods. The post-sunset peak in VTEC precedes the corresponding peak in airglow intensity. By comparing post-sunset VTEC enhancements with ionosonde observations from Tirunelveli (8.7°N, 77.7°E, dip angle 1.7°), it is shown that pre-reversal enhancement (PRE) of the zonal electric field causes these enhancements over the EIA crest region. These observations are supported by TEC measurements by GAGAN (GPS Aided Geo Augmented navigation), the Indian Satellite-based Augmentation System (SBAS). Comparison of average VTEC variations with global empirical model drifts reveals that the post-sunset enhancements in VTEC occurs ~1.7 h after the PRE and are significant only during December solstice and equinoctial months in high solar activity years similar to seasonal variations in PRE amplitudes. This time delay (response time of EIA crest) is almost half compared to the average response time (3–4 h) associated with the daytime fountain. Based on the latitudinal gradient in SBAS-TEC, it is proposed that the PRE drives plasma from 5°N to 10°N magnetic latitudes to the EIA crest region leading to shorter response time. These results show the important role of the PRE in conditioning the EIA crest region.

**Plain Language Summary** The equatorial ionization anomaly (EIA) crest region is one of the most important regions in the globe as far as the L-band scintillation during post-sunset hours is concerned. The plasma density variations over this region have important ramifications for the positional systems, navigation, and communication applications. Therefore, understanding the plasma density variations over this region during post-sunset hours is important. In this work, it is shown that the evening time electric field variations over the dip-equator changes the plasma density variations over the EIA crest region during post-sunset hours at a much faster time scale than what is expected based on daytime processes. The possible mechanism is discussed.

## 1. Introduction

The variability in the low latitude F region plasma distribution is greatly controlled by the equatorial F region plasma fountain process (Anderson, 1973a, 1973b). This process generates two ionization crests around ±15° geomagnetic latitudes and an ionization trough over the dip equator. This is known as equatorial ionization anomaly (EIA). Meridional winds cause asymmetry in the intensity and location of the EIA crest regions (e.g., Anderson, 1973a). The plasma distribution over the EIA crest regions shows day-to-day variability (e.g., Huang et al., 1989) as well as seasonal and solar activity dependences (e.g., Chakrabarty et al., 2012; Huang & Cheng, 1995; Mo et al., 2018). Understanding the plasma density variability over the EIA crest region is important as it is one of the most L-band scintillation affected regions in the globe (e.g.,

Basu et al., 1988). The L-band scintillation has ramifications for the positional systems, navigation, and communication applications.

It has been shown that the EIA crest region gets formed in the afternoon hours (e.g., Balan et al., 2018; Y. Chen et al., 2016; Mo et al., 2018; Sastri, 1990) during geomagnetically quiet periods. The time of occurrence of a well-developed EIA crest region during quiet period can, in general, be explained by adding a typical diffusion time of 3–4 h with the time of maximum eastward electric field over the dip equator around noon. Conventionally, the response time of the EIA crest region can be determined based on the time of occurrence of peak VTEC over the EIA crest region and the time of occurrence of peak vertical drift (present work) or EEJ strength (e.g., Rama Rao et al., 2006) or hmF2 (e.g., Aswathy et al., 2018). During the local evening hours, the eastward electric field in the equatorial F-region is greatly enhanced that is known as the pre-reversal enhancement (PRE) of the zonal electric field (e.g., Eccles et al., 2015; Fejer, 2011). As the amplitude of the PRE becomes comparable to the daytime maximum on occasions (e.g., Fejer et al., 2008), it is expected that the PRE should affect EIA crest region by re-invigorating the plasma fountain process. However, if one considers the duration of the PRE and 3–4 h of diffusion time (similar to daytime), the ionization over the EIA crest region is not expected to get affected by the PRE-driven fountain. This is because the equatorial zonal electric field changes to westward direction after the PRE and eventually reverse plasma fountain (e.g., Balan et al., 1995, 1997; C.-H. Chen et al., 2017; Sridharan et al., 1993; Yadav et al., 2020) sets in before the PRE-driven fountain can transport plasma from the dip equator to the crest region. Therefore, it is important to understand how much time the EIA crest region takes to respond to the PRE and how does it compare to the response time during daytime. Although several studies in the past reported (e.g., Bittencourt et al., 2007; Farelo et al., 2002; Rao & Kulkarni, 1973; Su et al., 1994; Xiong et al., 2016) conspicuous variations in the plasma density over the EIA crest region during post-sunset hours, the exact role of the PRE remains unclear. This important and unresolved scientific issue is addressed in the present work.

## 2. Data Set and Model

A narrow band and narrow field-of-view (bandwidth: 0.3 nm and field of view: 3°) airglow photometer was operated from Mt. Abu (24.6°N, 72.7°E, dip angle 38.0°), an EIA crest location, in campaign mode (operation during a specific period) in the winter months since 2013. The photometer was operated in moonless and cloudless nights to capture the variations in the OI 630.0 nm thermospheric airglow emission intensity. The details of this photometer are available in literature (e.g., Chakrabarty et al., 2008, 2015; Sekar & Chakrabarty, 2011). In the present work, airglow intensity data with 10 s cadence are used.

Vertical total electron content (VTEC) data from a dual frequency (L-band, 1575 and 1227 MHz) GPS receiver (GISTM GSV4004B) at Physical Research Laboratory (PRL), Ahmedabad (23.0°N, 72.6°E, dip angle 35.2°) during 2010–2019 are used in this work. The details of this receiver, the data analysis techniques are available in Manke and Chakarabarty (2016). Raypath elevation angles less than 30° are not considered in this work to minimize the multipath error and tropospheric scattering effects. Five minutes' average VTEC data are used for this study. Based on variations in F10.7 solar radio flux, the VTEC data during 2011–2015 are classified as belonging to high solar activity years and the rest of the data are categorized as falling in low solar activity years. Average F10.7 flux levels for high and low solar activity periods during 2010–2019 are ∼130 sfu and ∼80 sfu (sfu = solar flux unit, 1 sfu = $10^{-22}$ Wm$^{-2}$Hz$^{-1}$) respectively. In both the solar epochs, the VTEC data are further categorized into three seasons namely December solstice (November, December, January, and February), Equinox (March and April, September and October), and June solstice (May, June, July, and August). This work pertains to geomagnetically quiet periods. Quiet periods are selected based on $A_p$ index (based on $A_p \leq 15$ on the chosen day and the previous day).

The TEC maps generated from the ionospheric delay broadcast by Indian Satellite-based Augmentation System (SBAS) are used in the present work. Indian SBAS is known as GAGAN (GPS Aided Geo Augmented Navigation). The SBAS-GAGAN network has 13 ground stations that constitute an ionospheric grid with 5° separation between grid points. At each ionospheric grid point (IGP), TEC has been derived with ∼ 5 min cadence. The details of the GAGAN architecture are available in Sunda et al. (2015). GAGAN TEC maps are used to examine the latitudinal variation of F region plasma over the Indian sector.

Following the methodology of Rastogi and Patel (1975), systematic measurements of horizontal component (H) of geomagnetic field from a dip equatorial station Tirunelveli (TIR, 8.7°N, 77.7°E, dip angle 1.7°) and the off-equatorial station Alibag (ABG, 18.6°N, 72.9°E, dip angle 26.4°) over the Indian sector are used to calculate the strength of the equatorial electrojet (EEJ) given by $H_{EEJ} = \Delta H_{TIR} - \Delta H_{ABG}$. Here, $\Delta H$ represents the daytime instantaneous $H$ value corrected for the nighttime base value of $H$. The temporal cadence of EEJ data is 1 min. Integrated EEJ strength (in nT-h) is calculated between 0700 and 1700 LT.

The measurements of the bottomside F layer height ($h'F$, in km) by the Canadian Advanced Digital Ionosonde (CADI) over the dip equatorial station Tirunelveli are used in the present work. The details of the CADI system are discussed in MacDougall et al. (1995) and Sripathi et al. (2016). The temporal variation of $h'F$, $dh'F \, / \, dt = \left[ (h'F)_{t_2} - (h'F)_{t_1} \right] / \left[ t_2 - t_1 \right]$, during post-sunset hours is used as a proxy for the equatorial F region vertical drift (in m/s). In order to derive $dh'F/dt$, the $h'F$ values are first subjected to Savitzky-Golay (SG) algorithm (e.g., Savitzky & Golay, 1964) with 15% smoothing window as the data are slightly noisy. The smoothed $h'F$ data are then used to calculate the temporal derivative. The smoothing is done to suppress the fast fluctuations in $dh'F/dt$. The advantage of SG algorithm is its ability to smooth out fast fluctuations without causing significant distortion in the time series data. Further, since the derivation of electron density profiles from the CADI ionograms could not be done unambiguously, the correction for the chemical recombination is not incorporated in the derived drift. However, $h'F$ during PRE hours in high solar activity periods are mostly above 300 km. Hence the correction for the recombination effect is insignificant and can be neglected (e.g., Bittencourt & Abdu, 1981). On the other hand, $h'F$ during PRE hours in low solar activity periods can sometimes lie below 300 km. On those occasions, the real vertical drifts are smaller than calculated.

Since continuous vertical drift/electric field measurements are not available from Indian dip equatorial stations, the quiet time vertical drift outputs are generated using the global climatological model of Fejer et al. (2008). It has been shown earlier (e.g., Pandey et al., 2017) that the vertical drifts from this model represent the Indian sector well. The model outputs are generated for 75°E longitude corresponding to sfus of 130 and 80, respectively. It is also to be noted that the local time for all the data set used in this work is with respect to 75°E longitude (LT = UT + 5 h).

## 3. Results

Figures 1a and 1b depict the variations in 630.0 nm nightglow intensity (solid red line), VTEC (solid blue line), and EEJ strength (gray area) from 0600 LT to midnight on 29–30 November, 2013. Figures 1c–1f depict the same except for 03–04 December 2013 and 24–25 November 2014. In Figures 1a–1d, post-sunset enhancements in airglow intensity and VTEC are clearly seen during 1945–2045 LT. The daytime peak VTEC seems to vary in accordance with the integrated EEJ strength. However, the post-sunset enhancements in the airglow intensity and VTEC can be seen to be uncorrelated with the integrated EEJ strength (particularly, see Figures 1b and 1e). It is also clear from Figures 1a–1d and 1f that the airglow intensity enhancements over Mt. Abu start slightly earlier than the onset of increases in the VTEC over Ahmedabad during post-sunset hours (marked by orange vertical boxes). However, the peak in the airglow intensity occurs slightly later than the peak in VTEC. It is to be noted here that unlike the sharp airglow intensity peaks, VTEC variations are, in general, characterized by step-like increase followed by gradual decrease. The time corresponding to the peak VTEC is taken as the time corresponding to the end point of the step-like increase. In order to aid visual inspection, two vertical dashed lines are superimposed that mark the times corresponding to the onset of increase and peak of the airglow intensity. Further, it can be noticed in Figure 1e that although there is a peak in VTEC at ~1920 LT, there is no corresponding enhancement in airglow intensity. In contrast to Figure 1e, strong intensity peak is observed in Figure 1f. It can also be noticed that the enhancement in VTEC occurs slightly earlier in Figure 1e (~1920 LT) compared to Figure 1f (~2000 LT). This difference in timing makes the peak in VTEC to coincide with the sharp fall in the airglow intensity associated with the F-region sunset in Figure 1e. This is in contrast to Figure 1f when the peak in VTEC coincides with the inflection point when airglow intensity starts increasing again after the sharp fall associated with F region sunset.
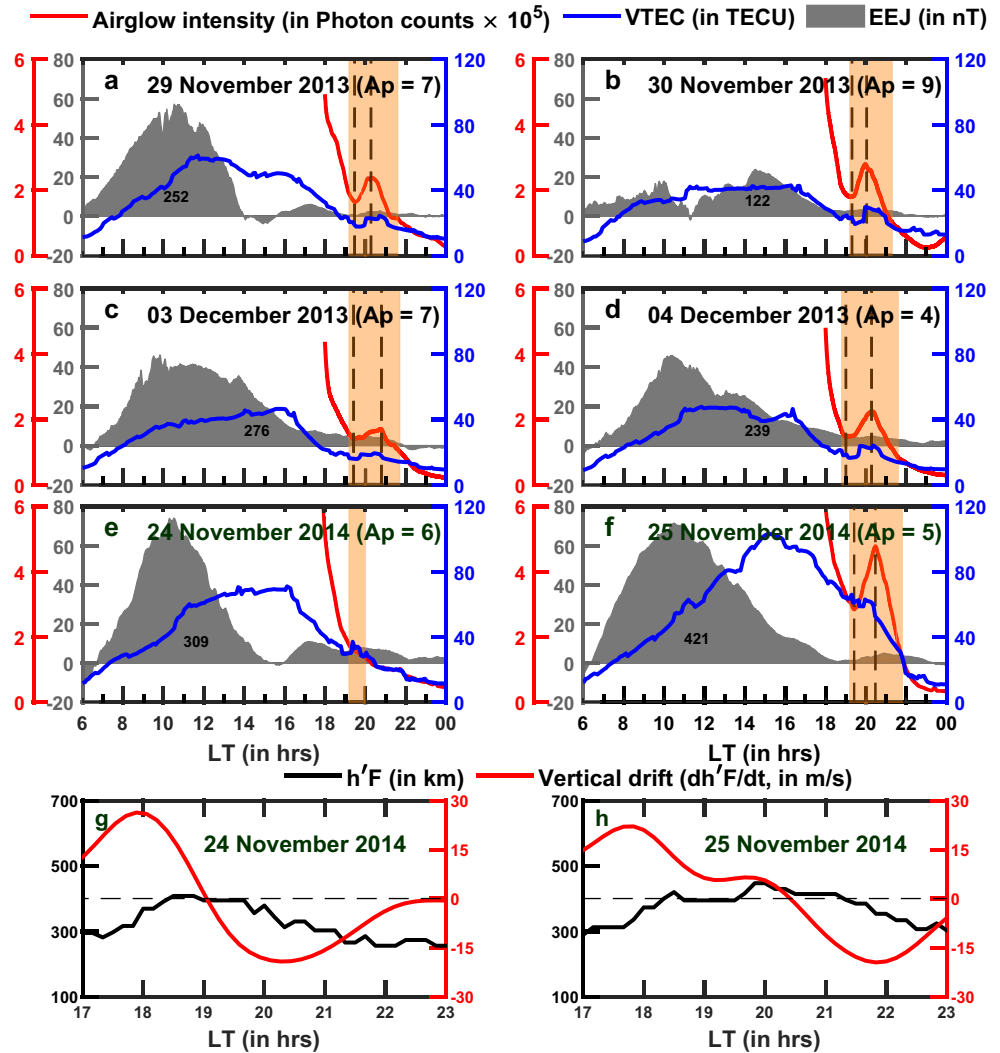
**Figure 1.** Variation of thermospheric OI 630.0 nm airglow intensity over Mt. Abu (red), VTEC over Ahmedabad (blue), and Equatorial electrojet (gray area) with local time on (a) 29 November 2013, (b) 30 November 2013, (c) 03 December 2013, (d) 04 December 2013, (e) 24 November 2014, and (f) 25 November 2014. Calculated integrated EEJ strength (numeric value) is written with black color over gray area. Virtual height-time-frequency plot from CADI measurement over Tirunelveli along with variation of bottomside F-layer height (black) and its derivative $dh'F/dt$ (red) with local time on (g) 24 November 2014, and (h) 25 November 2014.

Although airglow observations for a number of nights are available, two representative cases (24 and 25 November, 2014) of contrasting post-sunset variations in airglow intensity are selected for further investigations. Note that while post-sunset VTEC peaks are observed on both the days, the airglow intensity peak is significant on 25 November and almost absent on 24 November. In order to investigate the location of the base of F-layer and its vertical movement on 24 and 25 November 2014, the variations in $h'F$ and smoothed vertical drift ($dh'F/dt$) during 1700–2300 LT are shown with black and red lines respectively in Figures 1g and 1h. It can be noted that on 25 November, the PRE associated vertical drifts are upward for much longer duration compared to 24 November. The PRE sustains till ~1900 LT and ~2015 LT on 24 and 25 November, respectively. Impact of these differences in vertical drift on the VTEC and airglow enhancements over EIA crest region during post-sunset hours is provided in discussion section.

In order to explore the causal connection between the PRE and the post-sunset enhancement over the EIA crest region, Figure 2 is presented. In Figures 2a and 2b, two contrasting vertical drift scenarios during
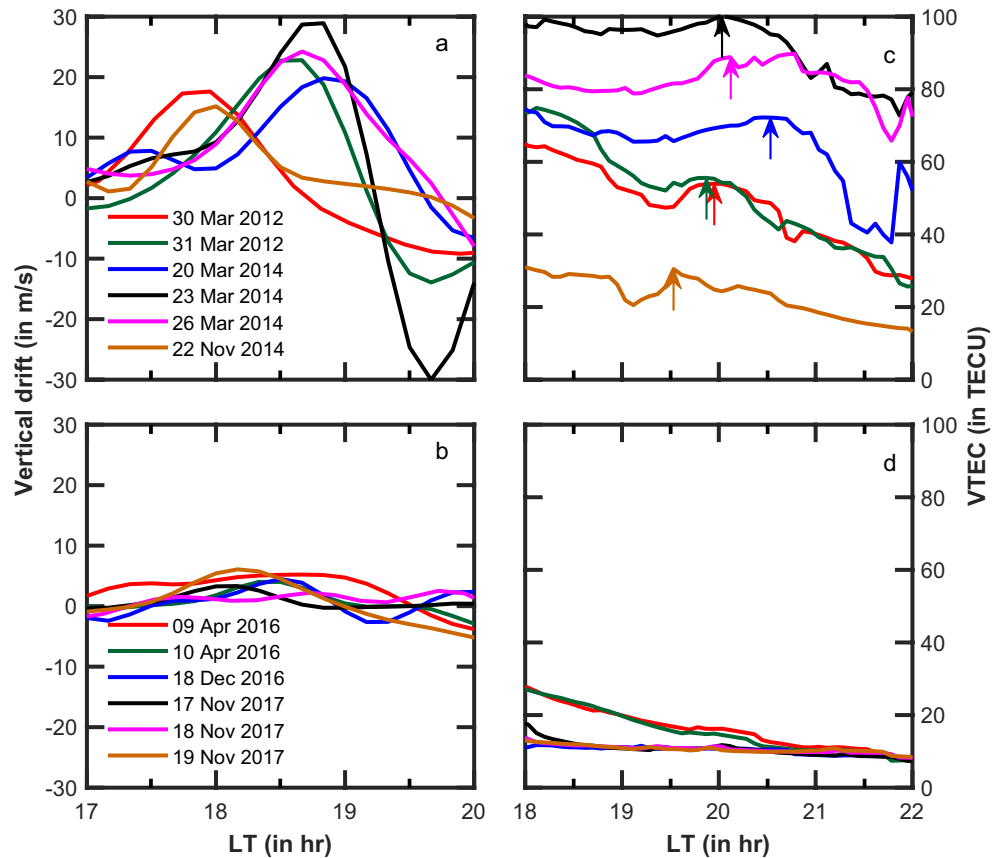
**Figure 2.** Variation of $dh'F/dt$ and VTEC is shown for the 30 March 2012 (red), 31 March 2012 (green), 20 March 2014 (blue), 23 March 2014 (black), 26 March 2014 (magenta), and 22 November 2014 (dark orange) in panels (a and c) respectively. The colored arrows indicate the time of occurrence of the peak VTEC. Similar variations on 09 April 2016 (red), 10 April 2016 (green), 18 December 2016 (blue), 17 November 2017 (black), 18 November 2017 (magenta), and 19 November 2017 (dark orange) are shown in panels (b and d).

1700–2000 LT are shown for six representative days. While Figure 2a shows the vertical drift variations with strong PRE features, Figure 2b reveals the variations when the PRE features are absent/subdued. Figures 2c and 2d represent the VTEC variations during 1800–2200 LT corresponding to Figures 2a and 2b, respectively. Interestingly, conspicuous enhancements in VTEC (peaks marked by colored arrows) can be noted in Figure 2c. On the other hand, Figure 2d is characterized by absence of any clear enhancement in VTEC. Therefore, the post-sunset enhancements in VTEC over the EIA crest region are observed whenever the PRE is strong over the dip equator. It is also important to note that the time delay between the peak vertical drift and post-sunset VTEC peak ranges from ∼1.4 h (31 March 2012) to ∼2 h (30 March 2012).

Figure 1 provides samples of day-to-day variability in the post-sunset enhancements in VTEC and airglow intensity over the EIA crest region. Figure 2 shows the connection between the PRE and the post-sunset enhancements in VTEC for a few representative cases. In Figure 3, the large database of VTEC are used in conjunction with model drifts to understand the seasonal and solar activity dependence of the post-sunset enhancement in VTEC over the EIA crest region (Ahmedabad). In Figures 3a–3f, VTEC variations for all the quiet days in three seasons during high (left column) and low (right column) solar activity years are shown (gray curves). The average variations in VTEC (black line) are overlaid on all these subplots. The average curves in Figures 3a–3f comprise of 428, 362, 450, 456, 327 and 317 days' of data. In addition, the vertical drift outputs from the Fejer et al. (2008) model (blue line) as well as smoothed $d(VTEC)/dt$ (red line) are superimposed on each subplot. The smoothed $d(VTEC)/dt$ is derived in the same way as has been adopted for vertical drift described earlier in Figures 1g and 1h. The peak VTEC values during noon (primary maximum) and post-sunset hours (secondary maximum) are identified by $P'$ and $S'$ respectively in the $d(VTEC)/$
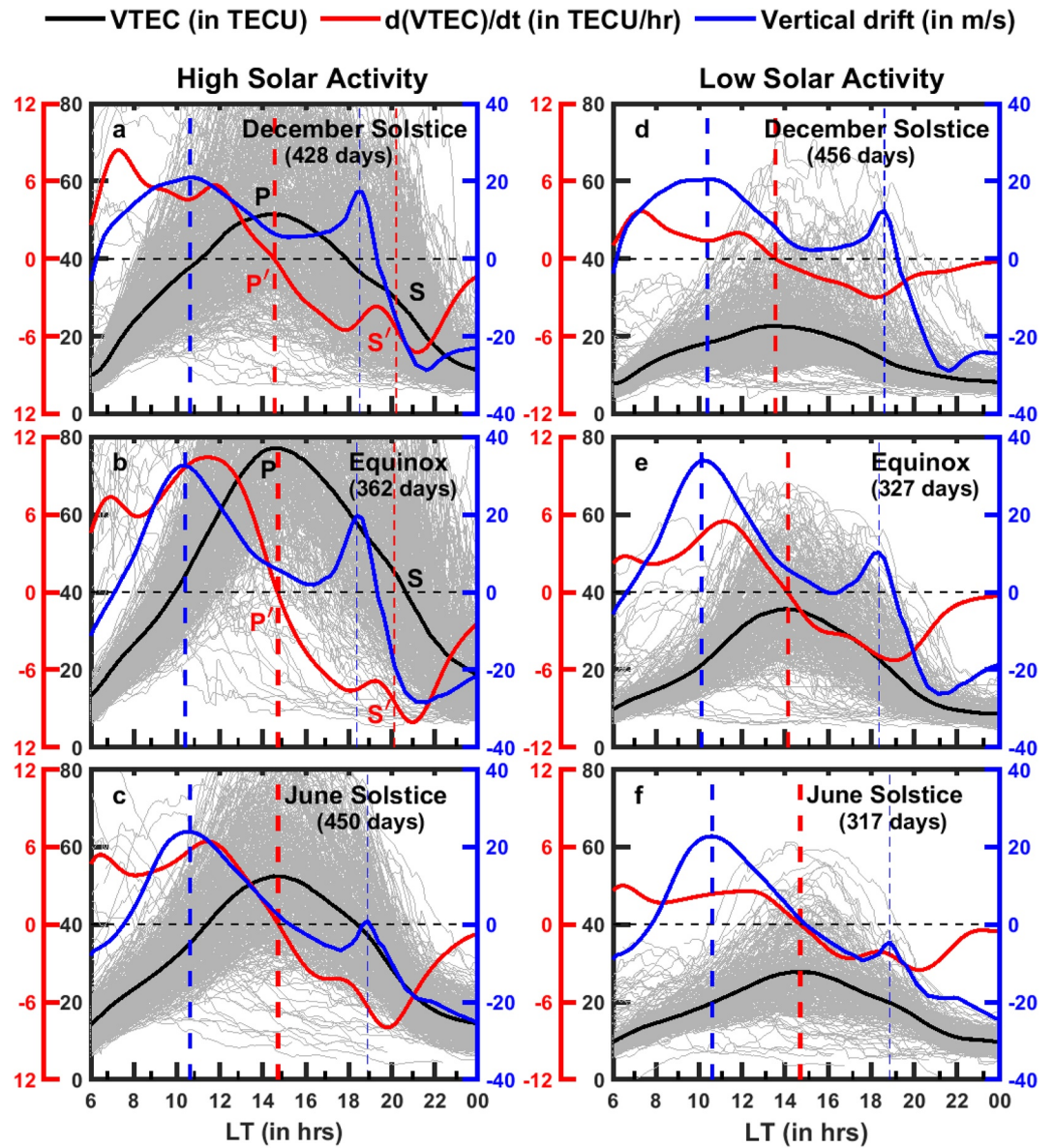
**Figure 3.** Variation of individual days' VTEC over Ahmedabad (gray), average of seasonal VTEC (black), temporal derivative of seasonal VTEC (red), and vertical drift (blue) in December solstice (top), Equinox (middle), and June solstice (bottom) under high (left panel) and low (right panel) solar activity years. The number of days used to calculate the seasonally averaged VTEC curve is also mentioned in each subplot. The points P and S represent primary (afternoon) and secondary (post-sunset) maxima of VTEC. P and S are determined based on P′ and S′ that are overall and local zero crossing points of $d$VTEC/$dt$. The intervals between the thick and thin vertical dashed lines (blue and red) are the response times of the EIA crest region during noon and post-sunset hours respectively.

$dt$ curves shown in Figures 3a and 3b. P′ is the point when $d$(VTEC)/$dt$ is zero indicating this is the time when primary maximum (daytime/overall maximum in VTEC) in VTEC is encountered. The trickier part is the S′ point based on which the secondary maximum (post-sunset peak) in VTEC is identified. Note that S′ is midway (local zero-crossing point) between the point when $d$(VTEC)/$dt$ starts increasing and the point when it returns back to the original variation. The P′ and S′ points help to identify the points P and S that are the maxima during noon and post-sunset hours. As the post-sunset increase in VTEC is embedded in the large amplitude diurnal variation, it is not immediately identifiable and hence, $d$(VTEC)/$dt$ helps to identify the VTEC peaks particularly the post-sunset one conspicuously. It is evident from Figure 3 that peak VTEC values are larger during high solar activity period. Interestingly, the enhancements in VTEC

during post-sunset hours (after the occurrence of the PRE) occur only in December solstice (Figure 3a) and Equinox (Figure 3b). The times of occurrence of daytime peaks in vertical drifts and VTEC are marked by thick vertical dashed lines in blue and red respectively. On the other hand, the PRE peak and peak of the post-sunset enhancement in VTEC are identified by thin vertical dashed line in blue and red respectively. It can be noted that while the daytime peaks in the VTEC occur during 1330–1500 LT for all seasons and solar epochs, the post-sunset peaks in VTEC occur at ~2000 LT in December solstice and Equinox during the high solar activity period only. Interestingly, the peak drifts during December solstice and Equinox occur at ~1830 LT. At this juncture, the response time of the EIA crest region can be defined as the interval between the time of occurrence of the peak drift (the daytime peak and the PRE-associated peak) and the peak VTEC (the points P and S). Going by this definition, it can be noted that the response time during afternoon hours is more than three hours. However, the response time during post-sunset hours are found to be applicable only during December solstice and Equinox in high solar activity epoch as post-sunset enhancements in VTEC are conspicuously observed after the PRE only for these two cases. The response times in these two cases is found out to be ~1.7 h. It is also to be noted that an evening peak in VTEC is also observed during June solstice in high solar epoch (Figure 3c). However, this peak occurs slightly before the PRE and it can be safely inferred that this peak is not causally related to the PRE. The physical mechanism for the generation of this VTEC peak is a subject matter of a separate investigation and will be taken up in future. Therefore, the response time of the EIA crest region during post-sunset hours is almost half compared to the response time during day.

Figure 4 depicts the SBAS-TEC maps around noon (first and third columns) and post-sunset hours (second and fourth columns) for 24 and 25 November 2014 respectively. Locations of Ahmedabad and Mt. Abu are marked by black (filled) circles in all the subplots. Local times are also shown in each subplot. Different color scales are chosen for all the four columns to bring out the large-scale plasma features conspicuously. It is striking to note that as time progresses in the afternoon hours, TEC gradually decreases over Mt. Abu/Ahmedabad on 24 November (Figures 4a–4d), whereas it gradually increases (Figures 4i–4l) on 25 November. Interestingly, during post-sunset hours on 24 November, TEC sharply decreases over the EIA crest region (Figures 4e–4h). However, on 25 November, the TEC values are comparatively larger over Ahmedabad and Mt. Abu till ~2100 LT (Figures 4m–4o). In fact, a very important feature that comes out after evaluating SBAS-TEC maps on many days during high solar activity period (not shown here) is that the daytime EIA crest becomes stronger (more TEC) over the Mt. Abu/Ahmedabad region during afternoon hours followed by a weakening (less TEC) in the evening hours. However, during post-sunset hours, TEC again increases (albeit in smaller degree) over this region followed by monotonic decrease during the nighttime. It is also to be noted that the post-sunset observations of TEC around Ahmedabad/Mt. Abu are mostly consistent with the post-sunset peak observed in airglow intensity on 24–25 November (Figures 1e and 1f).

Figure 5 is planned to bring out the latitudinal gradient in TEC during the intervals addressed in Figure 4. Figures 5a and 5c depict the latitudinal variations in SBAS-TEC along the 75°E longitude at multiple noon/afternoon (dashed lines) and post-sunset/pre-midnight (solid lines) local times on 24 and 25 November 2014 whereas Figures 5b and 5d show the same plots in normalized scales. TEC variations for each time is normalized with respect to the maximum TEC observed at that local time across all latitudes considered here. This is done to facilitate easy comparison of the latitudinal gradients in the TEC variation at different local times. The latitudes of Ahmedabad and Mt. Abu are shown with vertical thin and thick brown arrows respectively at the X-axes of each panel. TEC variations around noon (1105, 1202, 1300, and 1422 h) and sunset hours (1802, 1900, 2002, 2100, and 2202 h) are represented by dashed and solid lines (in different colors) respectively. From Figures 5b and 5d, the locations of the EIA crest region can be clearly identified at different local times. It can be noted from Figure 5, that the daytime latitudinal TEC gradients on the equatorial side of the EIA crests are much smaller than the post-sunset gradients on 25 November. It is also clear that TEC maximizes closer to the location of Ahmedabad/Mt. Abu (between 10° and 15°) on both 24 and 25 November during daytime. However, the nighttime EIA crest is located much closer to the dip-equator during the post-sunset hours on 24 November. In contrast, the crest location in post-sunset hours on 25 November is closer to the daytime crest location and moves toward the dip-equator around 2200 h (green solid line in Figure 5d). This is a classic example of the reverse fountain and this happens between 2100 and 2200 h. Most strikingly, the latitudinal gradient in TEC gradually becomes maximum during 2000–2100 h
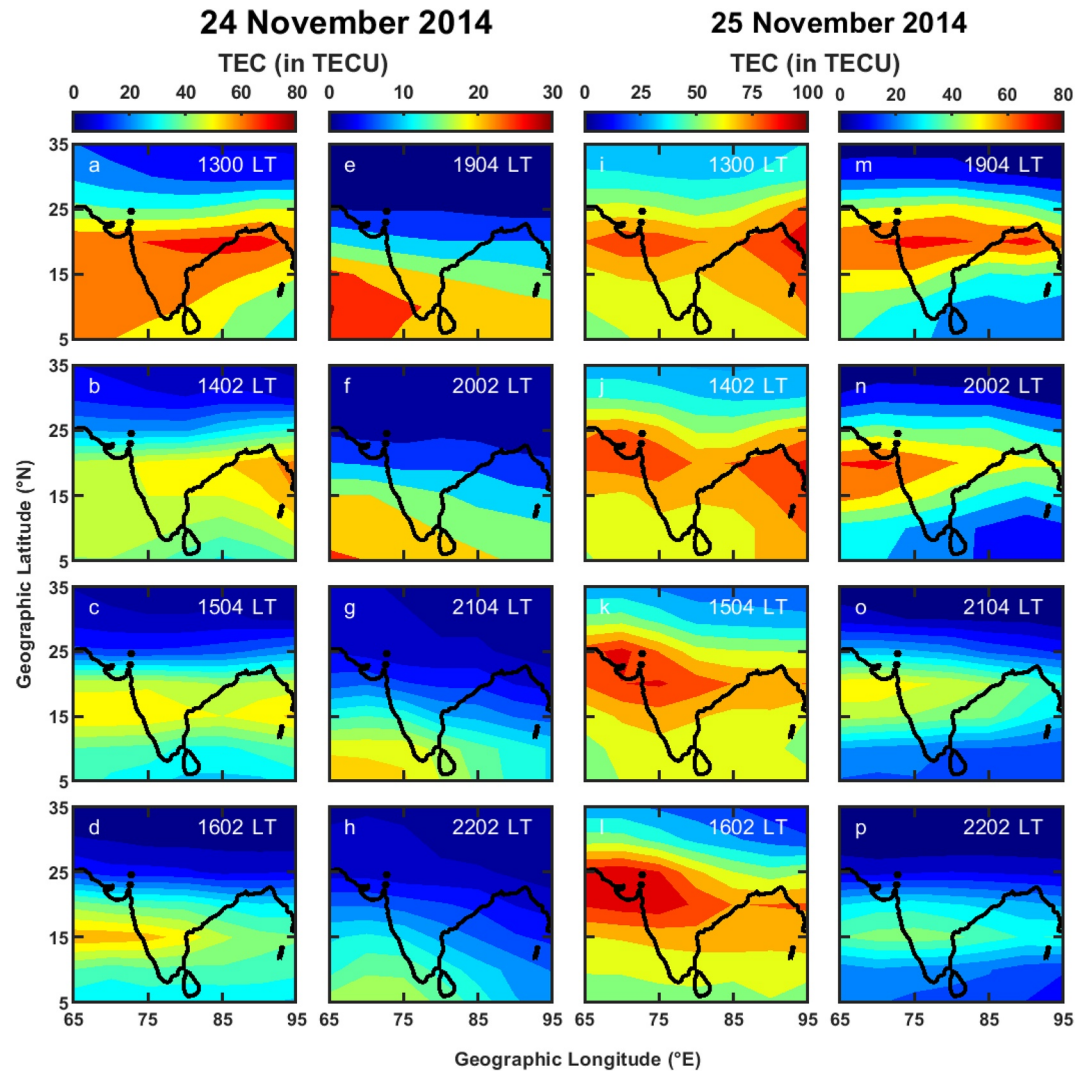
**Figure 4.** SBAS-TEC maps are shown for 24 November 2014 (a–h) and 25 November 2014 (i–p). Different color scales are adopted for all the four columns to make the large-scale plasma features conspicuous.

just before the reverse fountain process starts. The implications of these observations will be discussed in the ensuing section.

## 4. Discussion

Earlier observations (e.g., Bittencourt et al., 2007; Farelo et al., 2002; Kulkarni, 1969; Rao & Kulkarni, 1973; Su et al., 1994; Xiong et al., 2016) over the years reported post-sunset enhancements in the plasma density over the EIA crest region. However, the processes that drive and generate this enhancement remain unaddressed. It is obvious from Figures 1 and 4 that the post-sunset enhancement in airglow intensity and VTEC are not directly related to the daytime plasma fountain. Interestingly, the airglow intensity enhancements over Mt. Abu start slightly earlier than the onset of increases in the VTEC over Ahmedabad. This is probably due to the reversal of the vertical drift from upward to downward direction associated with the reversal in the zonal electric field. On careful scrutiny, one can note that the onset of increase in airglow intensity starts sometime during ~1900–1930 LT. This approximately coincides with the time of polarity reversal in the model vertical drift over the Indian dip equatorial station (indicated by Figures 3a and 3b). A downward drift supplies more plasma to the airglow emitting layer resulting in the onset of increase of airglow intensity at this time. As the downward drift does not change the total columnar content of electrons, the VTEC
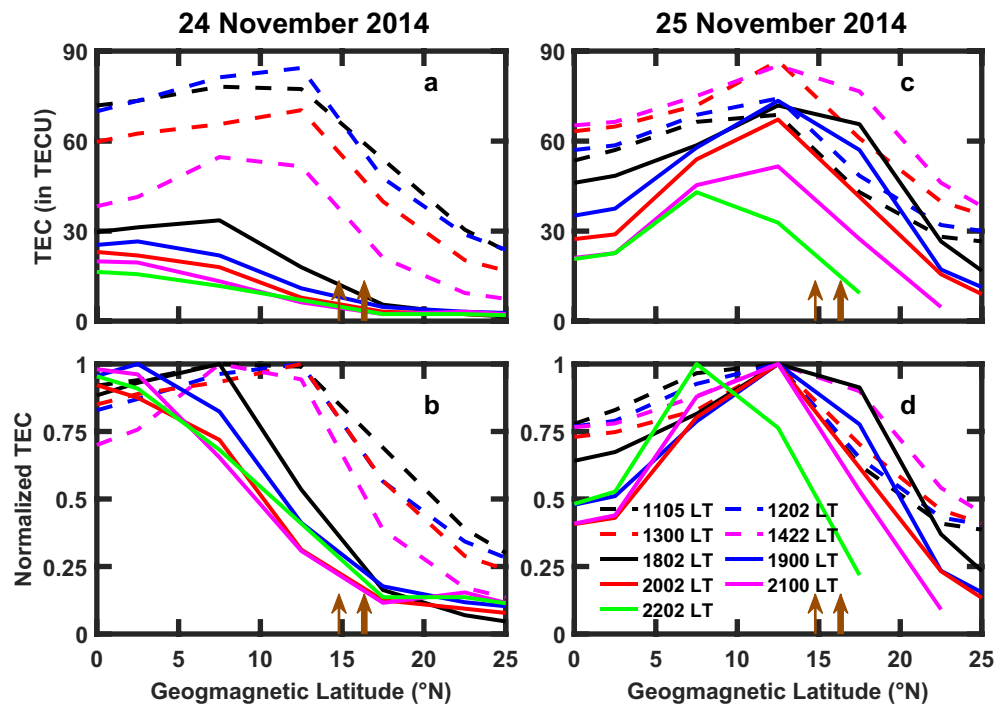
**Figure 5.** Panels (a) and (c) show the latitudinal variation of SBAS-TEC on 24 and 25 November 2014, respectively along 75°E geographic longitude (148°E geomagnetic longitude). Panels (b) and (d) represent the latitudinal variation of normalized SBAS-TEC corresponding to panels (a) and (b) respectively. Dashed and solid lines are used to show the variations during daytime (1105, 1202, 1300, and 1422 LT) and post-sunset hours (1802, 1900, 2002, 2100, and 2202 LT). Thin and thick brown arrows denote the latitudes of Ahmedabad and Mt. Abu, respectively.

remains unaffected. In fact, VTEC during post-sunset hours changes if there is a meridional transport of plasma. Therefore, the onset of the increase in VTEC marks the onset of arrival of additional plasma from meridional direction. In the intervening period between the onset of increase and the peak intensity, the airglow intensity variations are expected to be governed by both downward vertical drift and the meridional plasma transport. In addition, meridional wind and recombination chemistry can mask the enhancements in airglow intensity to a certain degree by contributing to vertical drift. Nevertheless, the peak in the airglow enhancement over Mt. Abu occurs at a slightly later time than the peak VTEC during post-sunset hours over Ahmedabad. During this time (2000–2030 LT), the changes in the downward drift are not significant as suggested by the model drifts in Figures 3a and 3b. Therefore, it is believed that both VTEC and airglow intensity enhancements at this time are governed by poleward plasma transport. This also rules out the role of reverse plasma fountain (e.g., Balan et al., 1997; Sridharan et al., 1993) that moves equatorward. Further, the reverse fountain over the EIA crest region reported by the earlier works suggests it's arrival at a later time compared to that of the post-sunset peak. This is supported by Figure 5d wherein the reverse fountain is detected sometime between 2100 and 2200 LT.

In order to explore the possible role of meridional wind, the outputs from the Horizontal Wind Model-14 (HWM-14, Drob et al., 2015) are evaluated (not shown here). These outputs as well as previous results (e.g., Balan et al., 1997; Drob et al., 2015) reveal that the poleward wind over the EIA crest region monotonically decreases during the time of occurrence of post-sunset enhancement in airglow intensity reported in this work. Under this condition, the poleward wind will be less efficient in pushing the plasma to the airglow emission altitude band centered at ~250 km. Therefore, the airglow intensity is expected to reduce monotonically during post-sunset hours. This is in contrast to the observations reported in the present work. Therefore, the role of poleward wind does not appear to be significant in this case. Nevertheless, the contribution of meridional wind along with others parameters is included in the subsequent paragraph to derive the parallel component of plasma diffusion velocity. It is also noteworthy that significant reduction in the amplitudes of the post-sunset VTEC peaks are seen during equinox in low solar activity years despite

similar magnitudes in the daytime peak eastward electric field (Figures 3b and 3e). Therefore, the direct role of daytime plasma fountain in causing the post-sunset VTEC enhancement over the EIA crest region can be ruled out.

Figure 2 firmly establishes the causal connection between the PRE and the post-sunset enhancements in VTEC over the EIA crest region. The representative cases shown in Figure 2 bring out the time delays between the peak vertical drift associated with the PRE and the peak VTEC that range from 1.4 to 2 h. These time delays are consistent with the average time delay between the PRE and post-sunset enhancement in VTEC over the EIA crest region shown in Figure 3. Interestingly, the post-sunset peaks appear only during December solstice and equinoctial months in high solar activity years and an enhanced PRE is a hallmark feature for these two seasons in high solar activity years (Fejer et al., 2008) as seen in Figure 3. This result is also consistent with the statistical work of Farelo et al. (2002) who showed that the amplitudes of the pre-midnight peak in NmF2 over low latitudes are most pronounced during winter solstice and Equinox in high solar activity years. It is to be noted that the PRE is subdued on other occasions and the significant post-sunset peaks in VTEC are also absent (Figure 3). Therefore, it follows that the PRE strengthens the plasma fountain in the post-sunset hours and this causes enhancements in VTEC and OI 630.0 nm airglow intensity over the EIA crest region with an average delay of ∼1.7 h.

The above understanding poses a conundrum. The post-sunset VTEC peak over the EIA crest region appears ∼1.7 h later than the time of occurrence of the PRE as opposed to the daytime peak VTEC that occurs 3–4 h after the daytime peak in equatorial vertical drift. It is to be noted in this context that not only the plasma response time (dip equator to crest) during day is consistent with the earlier works (e.g., Rama Rao et al., 2006) but the occurrence of minimum delay during December solstice in low solar activity years is also consistent with the observations made by Aswathy et al. (2018). Further, it may be noted here that observations from the Indian sector suggest that the PRE occurs about half an hour later in Equinox compared to December solstice (e.g., Madhav Haridas et al., 2015; Sripathi et al., 2016). This may reduce the response time of the EIA crest region during Equinox if one uses vertical drift observations from the dip equatorial station. Considering the objective of the present work is to show the reduced response time of the EIA crest region corresponding to the PRE, the conclusion drawn in this work regarding the reduced response time remains unaffected. In order to understand the significantly less response time of the EIA crest region during post-sunset hours, the parallel component ($V_\parallel$) of plasma diffusion velocity in the meridional direction is estimated assuming the perpendicular component ($V_\perp$) to be negligible over low latitudes. This is reasonable as, over low latitudes, contribution of $V_\perp$ to the crest-ward movement of plasma is expected to decrease as dip angle increases. $V_\parallel$ is calculated at 350 km height for three representative magnetic latitudes (5°N, 10°N, and 15°N) in December Solstice and Equinox based on the following equation (Anderson, 1971):

$$NV_\parallel = -D_a \left[ \frac{N sin I}{\epsilon H} + \frac{1}{\epsilon T_i} \left( sin I \frac{\partial(\epsilon N T_i)}{\partial N} + \frac{cos I}{r} \frac{\partial(\epsilon N T_i)}{\partial \theta} \right) \right] + N U_\theta cos I \tag{1}$$

In Equation 1, $N$, $I$, and $U_\theta$ represent the electron density, magnetic dip-angle, and meridional wind respectively. $T_e$ and $T_i$ denote electron and ion temperatures and $\epsilon = (T_e + T_i)/T_i$. $H$ and $D_a$ represent atomic Oxygen ion scale height and ambipolar diffusion coefficient respectively. The relevant plasma, neutral, geomagnetic field and meridional wind parameters used as inputs in Equation 1 are taken from IRI-16 (Bilitza et al., 2017), NRLMSISE-00 (Picone et al., 2002), IGRF-13 (Alken et al., 2021), and HWM-14 (Drob et al., 2015) models respectively. Interestingly, calculations based on Equation 1 reveals that $V_\parallel$ is smaller in post-sunset hours (∼45–55 m/s) compared to noon time (∼70–80 m/s) in December solstice. On the other hand, the $V_\parallel$ values during post-sunset and noon hours are ∼20 m/s in Equinox. This is primarily due to the weaker meridional wind during Equinox. This has been verified by HWM-14 model outputs (figure not shown here). Although $V_\parallel$ values are smaller in Equinox than December solstice during post-sunset hours, the enhancements in VTEC over EIA crest region occur around the same local time in these two seasons (Figures 3a and 3b). It is because the PRE occurs later in Equinox than December solstice (e.g., Madhav Haridas et al., 2015; Sripathi et al., 2016). These results suggest that the F-region background conditions over low latitude do not support the reduced response time of the EIA crest region during post-sunset hours.

The present work shows that not only the plasma concentration increases over the EIA crest region (Figure 4) but the latitudinal gradient also becomes much steeper during the post-sunset hours (Figure 5). It
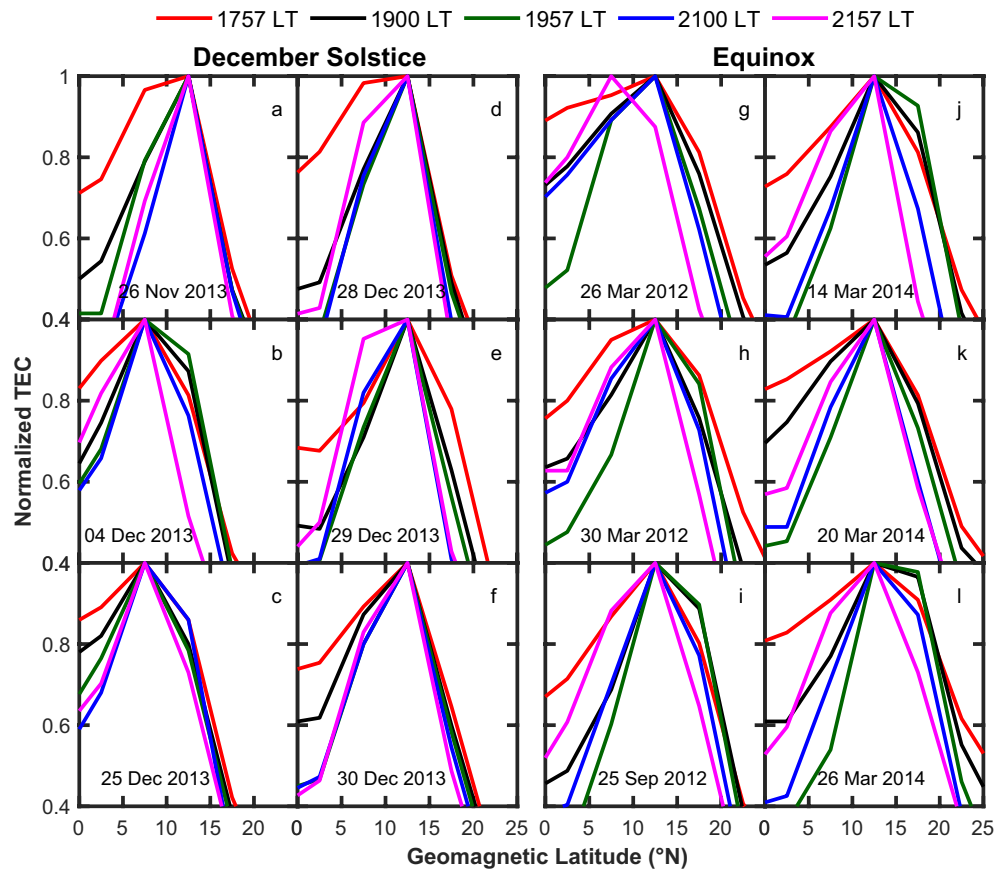
**Figure 6.** Variations of normalized SBAS-TEC with magnetic latitude (similar to Figures 5b and 5d) at 1757, 1900, 1957, 2100, and 2157 LT for six representative days during December solstice (a–f) and Equinox (g–l) are shown. It can be seen that the latitudinal gradient from 5°N to 10°N to the EIA crest region maximizes and then decays during the post-sunset hours.

is also verified that these results are consistent (not shown here) with the global GPS TEC maps (https://cdaweb.gsfc.nasa.gov/). Such an enhancement in TEC over EIA crest and depletion in the trough region during post-sunset hours can also be noticed in the earlier works corresponding to geomagnetically quiet (e.g., Figure 1 of C.-H. Chen et al., 2017) and disturbed periods (e.g., Figure 6 of Rout et al., 2019). A few earlier studies (e.g., Liu et al., 2007; Sunda & Vyas, 2013) have reported the crest to trough ratio to be larger during the post-sunset hours. Based on Sheffield University Plasmasphere Ionosphere Model (SUPIM), Balan et al. (1997) studied the equatorial plasma fountain under magnetically quiet equinoctial conditions in high solar activity period. Figure 4 of Balan et al. (1997) reveals that at the time of the PRE (1900 LT), the F region plasma gets transported to the EIA crest region from 5° to 10°N magnetic latitude. As the plasma transport from the dip equatorial region to EIA crest is expected to take 3–4 h, the post-sunset enhancement over EIA crest region is unlikely to have plasma contribution from latitudes closer to the dip equator. Owing to significant magnitude of $V_{\perp}$ till ~7.5° dip latitude (Fejer et al., 1995) plasma would primarily have vertical motions closer to the dip equator and would not get sufficient time to reach EIA crest region before electric field reversal. Therefore, it is evident that relative dominance ($V_{\parallel}$ becomes increasingly significant) of horizontal plasma transport from 5°N to 10°N causes the enhancement of VTEC and airglow intensity at the EIA crest region during post-sunset hours. As the latitudinal coverage is almost half, the time taken for the PRE-driven plasma to reach EIA crest region is also reduced almost by half. In order to confirm this proposition, the latitudinal TEC variations (normalized as in Figures 5b and 5d) on a large number of days have been investigated. Figure 6 shows the latitudinal TEC variations at five different local times (1757, 1900, 1957, 2100, and 2157 LT) separated by about an hour for six representative days during December solstice (Figures 6a–6f) and Equinox (Figures 6g–6l). It can be noted that the latitudinal gradient from 5°N to 10°N

to the EIA crest region keeps increasing in the post-sunset hours, maximizes sometime during 2000–2100 LT and decreases afterward. This strongly suggests plasma transport from low latitude to the EIA crest region during 2000–2100 LT resulting in steep latitudinal gradient in TEC. The fact that the latitudinal gradient decreases from 5°N to 10°N to the EIA crest region at ∼2200 LT suggests that the PRE-driven transport of plasma gets over by this time. It is intuitively obvious that had the plasma traveled from the dip equator to the EIA crest region, it would have taken similar time as it takes during day. The PRE driven plasma closer to the dip equator does not get that time as the reverse fountain starts around 2100 LT (Balan et al., 1997). Once the reverse fountain starts, the post-sunset enhancement in VTEC and airglow intensity starts weakening.

As a concluding remark, it can be said that if the plasma transport from 5°N to 10°N to the EIA crest region occurs during the sharp fall in airglow intensity in the evening hours associated with the F region sunset, the signature of the PRE driven fountain may not be conspicuous in airglow. This is because the rate of reduction in airglow intensity due to the F region sunset is drastic and it will obscure the enhancements due to the PRE (Figure 1e).

## 5. Summary

It is shown that the PRE of the equatorial zonal electric field causes the enhancement in the plasma density over the EIA crest region during post-sunset hours before the reverse fountain process comes into play. This effect is seen only during December solstice and equinoctial months in high solar activity years. It is proposed that plasma is transported from 5° to 10°N magnetic latitude to the EIA crest region. The response time of the EIA crest region corresponding to the PRE driven fountain is found to be almost half compared to that associated with daytime plasma fountain.

## Data Availability Statement

$A_p$ index data is taken from the World Data Center for Geomagnetism, Kyoto (http://wdc.kugi.kyoto-u. ac.jp/). F10.7 solar flux values are obtained from NASA GSFC CDAWeb (http://cdaweb.gsfc.nasa.gov/). The remaining data can be obtained from https://osf.io/mkg6b.

## References

Alken, P., Thebault, E., Beggan, C., Amit, H., Aubert, J., Baerenzung, J., et al. (2021). International geomagnetic reference field: The thirteenth generation. *Earth, Planets and Space*, *73*, 50.

Anderson, D. (1971). *Daily variation of the ionosphere F2 equatorial anomaly in the American & Asian sectors* (Unpublished doctoral dissertation). NCAR: University of Colorado and High Altitude Observatory.

Anderson, D. (1973a). A theoretical study of the ionospheric *F* region equatorial anomaly – I. Theory. *Planetary and Space Science*, *21*(3), 409–419. https://doi.org/10.1016/0032-0633(73)90040-8

Anderson, D. (1973b). A theoretical study of the ionospheric *F* region equatorial anomaly – II. Results in the American and Asian sectors. *Planetary and Space Science*, *21*(3), 421–442. https://doi.org/10.1016/0032-0633(73)90041-X

Aswathy, R. P., Manju, G., & Sunda, S. (2018). The response time of equatorial ionization anomaly crest: A unique precursor to the time of equatorial spread *F* initiation. *Journal of Geophysical Research: Space Physics*, *123*(7), 5949–5959. https://doi.org/10.1029/2018JA025469

Balan, N., Bailey, G., Abdu, M., Oyama, K., Richards, P., MacDougall, J., & Batista, I. (1997). Equatorial plasma fountain and its effects over three locations: Evidence for an additional layer, the *F₃* layer. *Journal of Geophysical Research*, *102*(A2), 2047–2056. https://doi.org/10.1029/95JA02639

Balan, N., Bailey, G., Moffett, R., Su, Y., & Titheridge, J. (1995). Modeling studies of the conjugate-hemisphere differences in ionospheric ionization at equatorial anomaly latitudes. *Journal of Atmospheric and Terrestrial Physics*, *57*(3), 279–292. https://doi.org/10.1016/0021-9169(94)E0019-J

Balan, N., Liu, L., & Le, H. (2018). A brief review of equatorial ionization anomaly and ionospheric irregularities. *Earth and Planetary Physics*, *2*(4), 257–275. https://doi.org/10.26464/epp2018025

Basu, S., MacKenzie, E., & Basu, S. (1988). Ionospheric constraints on VHF/UHF communications links during solar maximum and minimum periods. *Radio Science*, *23*(3), 363–378. https://doi.org/10.1029/RS023i003p00363

Bilitza, D., Altadill, D., Truhlik, V., Shubin, V., Galkin, I., Reinisch, B., & Huang, X. (2017). International reference ionosphere 2016: From ionospheric climate to real-time weather predictions. *Space Weather*, *15*(2), 418–429. https://doi.org/10.1002/2016SW001593

Bittencourt, J. A., & Abdu, M. A. (1981). A theoretical comparison between apparent and real vertical ionization drift velocities in the equatorial *F* region. *Journal of Geophysical Research*, *86*(A4), 2451–2454. https://doi.org/10.1029/JA086iA04p02451

Bittencourt, J. A., Pillat, V. G., Fagundes, P. R., Sahai, Y., & Pimenta, A. A. (2007). LION: A dynamic computer model for the low-latitude ionosphere. *Annales Geophysicae*, *25*(11), 2371–2392. https://doi.org/10.5194/angeo-25-2371-2007

Chakrabarty, D., Bagiya, M. S., & Thampi, S. V. (2012). Solar EUV flux (0.1-50 nm), F10.7 cm flux, sunspot number and the total electron content in the crest region of equatorial ionization anomaly during the deep minimum between solar cycle 23 and 24. *Indian Journal of Radio and Space Physics*, *41*(2), 110–120.

Chakrabarty, D., Rout, D., Sekar, R., Narayanan, R., Reeves, G. D., Pant, T. K., et al. (2015). Three different types of electric field disturbances affecting equatorial ionosphere during a long-duration prompt penetration event. *Journal of Geophysical Research: Space Physics*, *120*(6), 4993–5008. https://doi.org/10.1002/2014JA020759

Chakrabarty, D., Sekar, R., Sastri, J. H., & Ravindran, S. (2008). Distinctive effects of interplanetary electric field and substorm on nighttime equatorial *F* layer: A case study. *Geophysical Research Letters*, *35*, L19108. https://doi.org/10.1029/2008GL035415

Chen, C.-H., Lin, C., Chen, W.-H., & Matsuo, T. (2017). Modeling the ionospheric prereversal enhancement by using coupled thermosphere-ionosphere data assimilation. *Geophysical Research Letters*, *44*(4), 1652–1659. https://doi.org/10.1002/2016GL071812

Chen, Y., Liu, L., Le, H., Wan, W., & Zhang, H. (2016). Equatorial ionization anomaly in the low-latitude topside ionosphere: Local time evolution and longitudinal difference. *Journal of Geophysical Research: Space Physics*, *121*(7), 7166–7182. https://doi.org/10.1002/2016JA022394

Drob, D. P., Emmert, J. T., Meriwether, J. W., Makela, J. J., Doornbos, E., Conde, M., et al. (2015). An update to the Horizontal Wind Model (HWM): The quiet time thermosphere. *Earth and Space Science*, *2*(7), 301–319. https://doi.org/10.1002/2014EA000089

Eccles, J. V., St Maurice, J. P., & Schunk, R. W. (2015). Mechanisms underlying the prereversal enhancement of the vertical plasma drift in the low-latitude ionosphere. *Journal of Geophysical Research: Space Physics*, *120*(6), 4950–4970. https://doi.org/10.1002/2014JA020664

Farelo, A. F., Herraiz, M., & Mikhailov, A. V. (2002). Global morphology of night-time NmF2 enhancements. *Annales Geophysicae*, *20*(11), 1795–1806. https://doi.org/10.5194/angeo-20-1795-2002

Fejer, B. G. (2011). Low latitude ionospheric electrodynamics. *Space Science Reviews*, *158*(1), 145–166.

Fejer, B. G., de Paula, E. R., Heelis, R. A., & Hanson, W. B. (1995). Global equatorial ionospheric vertical plasma drifts measured by the AE-E satellite. *Journal of Geophysical Research*, *100*(A4), 5769–5776. https://doi.org/10.1029/94JA03240

Fejer, B. G., Jensen, J. W., & Su, S.-Y. (2008). Quiet time equatorial *F* region vertical plasma drift model derived from ROCSAT-1 observations. *Journal of Geophysical Research*, *113*, A05304. https://doi.org/10.1029/2007JA012801

Huang, Y.-N., & Cheng, K. (1995). Solar cycle variation of the total electron content around equatorial anomaly crest region in East Asia. *Journal of Atmospheric and Terrestrial Physics*, *57*(12), 1503–1511. https://doi.org/10.1016/0021-9169(94)00147-G

Huang, Y.-N., Cheng, K., & Chen, S. W. (1989). On the equatorial anomaly of the ionospheric total electron content near the northern anomaly crest region. *Journal of Geophysical Research*, *94*(A10), 13515–13525. https://doi.org/10.1029/JA094iA10p13515

Kulkarni, P. V. (1969). Airglow studies in low latitudes. *Presented at Third International Symposium on Equatorial Aeronomy*, *2*(1), 412.

Liu, H., Stolle, C., Frster, M., & Watanabe, S. (2007). Solar activity dependence of the electron density in the equatorial anomaly regions observed by champ. *Journal of Geophysical Research*, *112*, A11311. https://doi.org/10.1029/2007JA012616

MacDougall, J., Grant, I., & Shen, X. (1995). The Canadian advanced digital ionosonde: Design and results. *URSI INAG Ionospheric Station Inf. Bulletin, UAG-104*.

Madhav Haridas, M. K., Manju, G., & Pant, T. K. (2015). On the solar activity variations of nocturnal *F* region vertical drifts covering two solar cycles in the Indian longitude sector. *Journal of Geophysical Research: Space Physics*, *120*(2), 1445–1451. https://doi.org/10.1002/2014JA020561

Manke, A. A., & Chakarabarty, D. (2016). An integrated software platform for GPS/GNSS ionospheric data analysis. *International Journal of Science, Engineering and Technology*, *4*(5), 796–804. https://doi.org/10.2348/ijset09160796

Mo, X. H., Zhang, D. H., Liu, J., Hao, Y. Q., Ye, J. F., Qin, J. S., et al. (2018). Morphological characteristics of equatorial ionization anomaly crest over nanning region. *Radio Science*, *53*(1), 37–47. https://doi.org/10.1002/2017RS006386

Pandey, K., Sekar, R., Gupta, S., Chakrabarty, D., & Anandarao, B. (2017). Comparison of quiet time vertical plasma drifts with global empirical models over the Indian sector: Some insights. *Journal of Atmospheric and Solar-Terrestrial Physics*, *157–158*, 42–54. https://doi.org/10.1016/j.jastp.2017.03.012

Picone, J. M., Hedin, A. E., Drob, D. P., & Aikin, A. C. (2002). NRLMSISE-00 empirical model of the atmosphere: Statistical comparisons and scientific issues. *Journal of Geophysical Research*, *107*, 1468. https://doi.org/10.1029/2002JA009430

Rama Rao, P. V. S., Gopi Krishna, S., Niranjan, K., & Prasad, D. S. V. V. D. (2006). Temporal and spatial variations in TEC using simultaneous measurements from the Indian GPS network of receivers during the low solar activity period of 2004–2005. *Annales Geophysicae*, *24*(12), 3279–3292. https://doi.org/10.5194/angeo-24-3279-2006

Rao, V., & Kulkarni, P. (1973). 6300 Å night airglow enhancements in low latitudes. *Journal of Atmospheric and Terrestrial Physics*, *35*(2), 193–206. https://doi.org/10.1016/0021-9169(73)90087-1

Rastogi, R., & Patel, V. (1975). Effect of interplanetary magnetic field on ionosphere over the magnetic equator. *Proceedings of the Indian Academy of Sciences-Section A*, *82*, 121–141. https://doi.org/10.1007/BF03046722

Rout, D., Pandey, K., Chakrabarty, D., Sekar, R., & Lu, X. (2019). Significant electric field perturbations in low latitude ionosphere due to the passage of two consecutive ICMEs during 6–8 September 2017. *Journal of Geophysical Research: Space Physics*, *124*(11), 9494–9510. https://doi.org/10.1029/2019JA027133

Sastri, J. H. (1990). Equatorial anomaly in *F*-region – A review. *Indian Journal of Radio and Space Physics*, *19*(4), 225–240.

Savitzky, A., & Golay, M. J. (1964). Smoothing and differentiation of data by simplified least squares procedures. *Analytical Chemistry*, *36*(8), 1627–1639.

Sekar, R., & Chakrabarty, D. (2011). A review of the recent advances in the investigation of equatorial spread F and space weather effects over Indian sector using optical and other techniques. In M. A. Abdu, & D. Pancheva (Eds.), *Aeronomy of the Earth's Atmosphere and Ionosphere* (pp. 251–268). Springer.

Sridharan, R., Sekar, R., & Gurubaran, S. (1993). Two-dimensional high-resolution imaging of the equatorial plasma fountain. *Journal of Atmospheric and Terrestrial Physics*, *55*(13), 1661–1665. https://doi.org/10.1016/0021-9169(93)90170-4

Sripathi, S., Singh, R., Banola, S., Sreekumar, S., Emperumal, K., & Selvaraj, C. (2016). Characteristics of the equatorial plasma drifts as obtained by using Canadian Doppler ionosonde over southern tip of India. *Journal of Geophysical Research: Space Physics*, *121*(8), 8103–8120. https://doi.org/10.1002/2016JA023088

Su, Y., Bailey, G., & Balan, N. (1994). Night-time enhancements in TEC at equatorial anomaly latitudes. *Journal of Atmospheric and Terrestrial Physics*, *56*(12), 1619–1628. https://doi.org/10.1016/0021-9169(94)90091-4

Sunda, S., Sridharan, R., Vyas, B. M., Khekale, P. V., Parikh, K. S., Ganeshan, A. S., & Bagiya, M. S. (2015). Satellite-based augmentation systems: A novel and cost-effective tool for ionospheric and space weather studies. *Space Weather*, *13*(1), 6–15. https://doi.org/10.1002/2014SW001103

Sunda, S., & Vyas, B. M. (2013). Local time, seasonal, and solar cycle dependency of longitudinal variations of TEC along the crest of EIA over India. *Journal of Geophysical Research: Space Physics*, *118*(10), 6777–6785. https://doi.org/10.1002/2013JA018918

Xiong, C., Zhou, Y.-L., Lhr, H., & Ma, S.-Y. (2016). Diurnal evolution of the $F$ region electron density local time gradient at low and middle latitudes resolved by the Swarm constellation. *Journal of Geophysical Research: Space Physics*, *121*(9), 9075–9089. https://doi.org/10.1002/2016JA023034

Yadav, S., Choudhary, R. K., Kumari, J., Sunda, S., Shreedevi, P. R., & Pant, T. K. (2020). Reverse fountain and the nighttime enhancement in the ionospheric electron density over the equatorial region: A case study. *Journal of Geophysical Research: Space Physics*, *125*, e2019JA027286. https://doi.org/10.1029/2019JA027286